Viscoelasticity and energy dissipation as indicators of flexural fatigue behavior in a ductile carbon fiber-reinforced cementitious composite

Matthias Rutzen, Dirk Volkmer *

Chair of Solid State and Materials Chemistry, University of Augsburg, Augsburg 86159, Germany

1. Introduction

Cementitious materials reinforced with chopped fibers can show different kinds of mechanical properties, depending on the interaction of the reinforcing fiber with the surrounding cementitious matrix. Often, fibers are found to merely increase the postfailure toughness of the material without impacting flexural or tensile strength by a large margin. These kinds of composites often employ macrofibers (diameter on the mm scale) with subcritical fiber lengths or weak interfacial bonds between the fiber and matrix, meaning that tensile loads cannot fully transition into the fiber before the matrix fails. Thus, the fibers mainly contribute to the mechanical behavior by being pulled out, leaving much of their tensile strength unused. Such systems are typically given the name 'fiber-reinforced concrete' (FRC) [1].

If fiber–matrix interactions are fine-tuned on a micromechanical level, a special type of composite can be created that allows fibers to bridge cracks in the matrix [2,3]. Once the composite is loaded past its linear-elastic deformation capacity, a multitude of small and stable cracks will appear in the specimen. This multiple cracking is caused by the briding action of the fibers which allows for transferring the load further along the specimen. The process of crack initiation and briding will repeat until the specimen is saturated with stable cracks. For the purpose of this manuscript, these small and stable cracks will be referred to as microcracks. This process causes strain-hardening behavior and significant pseudoductility in the material. The specimen will be able to handle a further increasing load, albeit at decreased stiffness. This process continues until one of the microcracks is loaded past its point of critical stress intensity, after which failure will occur [4]. Fig. 1 shows typical stress–strain diagrams of such a composite in contrast to the behavior of an unreinforced matrix.

Composites showing this kind of behavior have been dubbed 'engineered cementitious composites' (ECCs) or, more recently, 'strain-hardening cementitious composites' (SHCCs) [5,6]. The main type of fibers used in such systems are polymer microfibers (diameter approximately 10 μm), usually made from high-density polyethylene (HDPE) or polyvinyl alcohol (PVA). Specimens reinforced in such a way show improved tensile properties and a deformation capacity of several percent. In addition to the increase in tensile and flexural strength, the small crack width is correlated with several other advantages. Research indicates that such composites can possess self-healing properties [7–9] as well as better overall durability, as the diffusion of aggressive substances is reduced by a small crack width [10].

Recent research has shown that such strain-hardening systems can also be produced by reinforcement with carbon fibers [11,12]. Using an extrusion process, a composite with controlled fiber alignment can be created. As they flow through the tight extrusion nozzle, the fibers will align themselves in the direction of the flow [13]. Thus, for the case of a moving extrusion system, fiber alignment will follow the direction in which the nozzle is moving. This process is shown in Fig. 2 for the case of manual extrusion through the nozzle of a syringe. By using strong and stiff carbon fibers, specimens with a flexural strength of more than 100 MPa and a strain-at-break value of 1.2% can be produced. The extrusion

* Corresponding author.
E-mail address: dirk.volkmer@physik.uni-augsburg.de (D. Volkmer).

technique has been successfully translated into an automated freeform 3D-printing process, making the composite an enticing material for lightweight, thin-walled elements [14]. Similar processes have also been realized using fiber-reinforced polymer resin [15] and calcium aluminate cement [16]. The automated manufacturing process potentially allows for matching fiber alignment with predicted loading scenarios [17]. Electrically conductive carbon fibers also offer the possibility to monitor the structural health of the composite or use it as a heating element [18,19].

While the behavior of these materials under static loading regimens is relatively well researched and understood, the number of publications describing cyclical load and failure by fatigue lags strongly behind, leaving the driving mechanisms less known [6,20,21]. Cementitious materials with carbon fiber reinforcement are increasingly regarded as a suitable material for thin-walled lightweight structural members [22,23]. As such lightweight structures are inherently more susceptible to oscillatory loads in contrast to more traditional masonry work, the question of how they are impacted by fatigue becomes increasingly important.

Common parameters used for the analysis of fatigue damage are the development of strain, Young's modulus and amount of dissipated energy during the test. The development of these parameters during cyclic loading typically shows 3 phases. Typical examples of how the respective parameters change during cyclic loading are shown in Fig. 3. For cementitious materials, phases 1 and 3 are often cited to each take up between 10% and 20% of the duration of the test [24]. Both phases are characterized by sudden changes in the respective parameters, whereas phase 2 is characterized by only a small and constant rate of change. This results in S-shaped curves for the development of strain and Young's modulus and U-shaped curves in the case of the energy dissipation rate [25–29]. Similar to fracture mechanics under static load, Paris and Erdogan correlated these phases to crack initiation (phase 1), stable crack growth (phase 2) and unstable crack growth with rapid failure (phase 3) [30]. While this general behavior is overwhelmingly likely to also apply to fiber-reinforced materials, these models use a linear-elastic material response with a single crack at failure as their framework. In the case of fiber-reinforced composites, further influences of effects such as multiple cracking and fiber–matrix interactions will have to be considered.

While fiber reinforcement is generally viewed as being beneficial to fatigue resistance, some contradicting trends can be found in the literature [31,32]. As the final performance of a composite depends on a multitude of factors, such as the mixture design of the cementitious material, type of fiber, fiber–matrix interaction, and flaws such as pores and fiber alignment, scattering must be expected. To gather as much information on possible influences not immediately visible to the naked eye, we aim to take a microstructure-based approach in this publication. In addition to purely observing common macroscopic fatigue damage indicators such as cycles to failure and strain development, fiber alignment and development of microcracks during cyclical loading are inspected using X-ray 3D computed tomography (X-ray CT) in miniature prisms put under a 3-point flexural load. To achieve satisfactory image resolution (approximately 1 μm – 2 μm to capture microcracks and fibers), the specimen geometry has to remain small. Such small specimens will show failure under very low force, making standard load cells used in universal testing machines potentially unreliable. Instead, we aim to introduce a dynamic mechanical analyzer (DMA) as a viable method of fatigue testing. Such machines are widely used for the analysis of the temperature-dependent properties of thermoplastic materials. As these types of machines do not focus on destructive testing, they are specifically built for usage at low oscillating forces (typically below 100 N). A further goal is to link the analysis of viscoelastic parameters that a DMA can provide to the fatigue process occurring in our fiber-reinforced composites as well as suggest connections to the more traditionally used parameters in fatigue testing, such as those shown in Fig. 3.

2. Materials and methods

2.1. Sample preparation

Samples were produced according to a mixture design introduced in previous publications of our group [11,12]. All raw materials and their proportions in the mixture design are given in Table 1.

The CEM I 52.5 R was supplied by Schwenk Zement KG (Ulm, Germany) and sourced from the cement plant located in Karlsstadt. Chopped carbon fibers were bought from Teijin Ltd. (Tokyo, Japan) under the

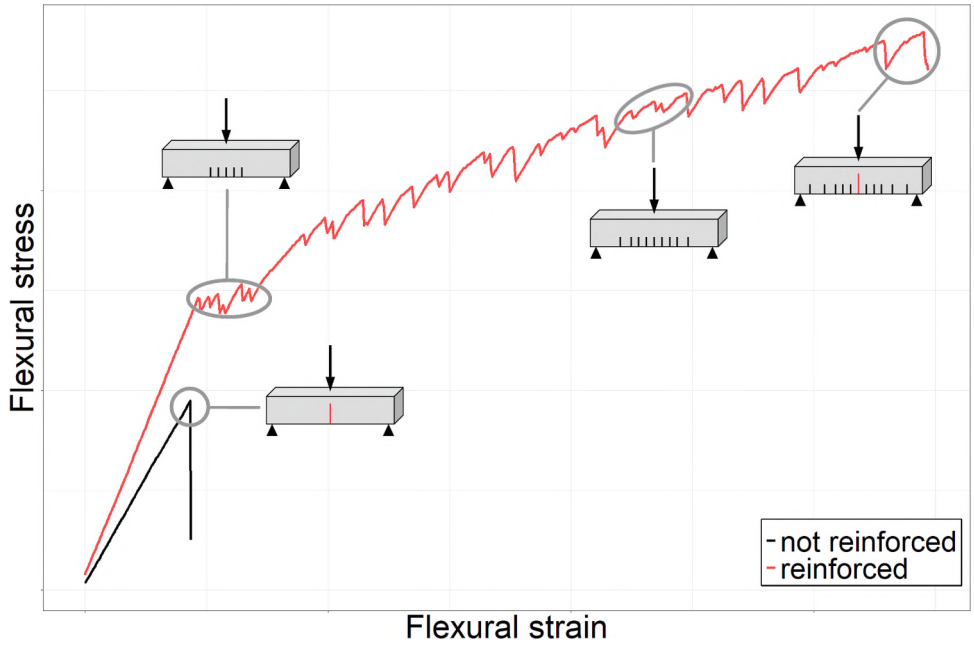

Fig. 1. Behavior of unreinforced cementitious materials (black) and SHCC materials (red) under flexural load. While unreinforced cementitious materials fail in a brittle fashion once a single critical crack has been introduced, reinforced composites will show stable multiple cracking before final failure. (For interpretation of the references to colour in this figure legend, the reader is referred to the web version of this article.)

brand name 'Tenax-J HT C261'. The fibers conformed to the following specifications: length: 3 mm, diameter: 7 μm, Young's modulus: 238 GPa, tensile strength: 4000 MPa. Fibers were desized and given an oxidative surface treatment in a furnace at 425 °C for 2 h to increase wettability and dispersion in the aqueous cement paste (see also Ref. [11]). Barium sulfate (Acros Organics, Geel, Belgium) is added for the purpose of raising the X-ray absorption of the matrix and thus allows for better contrast between the lower density fibers and other inclusions [33].

Cement, barium sulfate and silica fume (brand name 'EFACO', produced by Egyptian Ferro-Alloys Company, Cairo, Egypt) were manually premixed in the dry state after being given into the mixing container. Directly after adding water and superplasticizer (brand name 'MasterGlenium ACE 430', Master Builders Solutions Deutschland GmbH, Trostberg, Germany), the paste was mixed using a Heidolph Hei-TORQUE Precision 400 overhead laboratory mixer (Heidolph Instruments GmbH & Co. KG, Schwabach, Germany) at 400 RPM for 90 s. Undispersed remains were cleaned from the container walls with a stirring tool and put back into the paste. Final homogenization was performed at 2000 RPM for 90 s. After the paste was properly homogenized, the carbon fibers were integrated at 70 RPM for 30 s.

The paste was filled into a 10 ml disposable syringe (B. Braun Melsungen AG, Melsungen, Germany, diameter of the nozzle: 2 mm) and extruded into rectangular molds measuring 3 mm × 13 mm × 60 mm. The specimens were left to harden in sealed desiccators for 28 days at room temperature under the following conditions:

- Day 1: Storage over water at 100% relative humidity
- Day 2 – Day 7: Underwater storage
- Day 8 – Day 28: Storage over oversaturated sodium bromide solution at 59% relative humidity

At Day 8, the surface of rectangular specimens was deburred and ground planed using a mounted Makita GD800C die grinder (Makita Corp., Anjo, Japan) with a diamond grinding point. After this, they were cut down into their final shape, resembling miniature prisms measuring 2 mm × 2 mm × 60 mm using a Buehler IsoMet low-speed saw (Buehler Ltd., Lake Bluff, IL, USA) with a diamond sectioning blade and stored until testing.

2.2. Mechanical testing

All mechanical tests were performed using a TA Instruments Q800 DMA (TA Instruments Inc., New Castle, DE, USA) with a sample holder for a 3-point-bending setup installed. The sample holder uses a fixed loading span of 50 mm. A photograph of the full 3-point-bending setup with a miniature prism can be seen in Fig. 4. Before measurement, the machine was calibrated to recognize the sample holder's weight and compliance and to calculate the results accordingly.

2.3. Determination of static flexural strength

Measurement of the static flexural strength $f_{ct,fl}$ was carried out using DMA's 'stress/strain controlled force' mode. Samples were loaded using a controlled force measurement at a rate of 1 N/min until failure. Flexural stress σ_{fl} is calculated according to:

$$\sigma_{fl} = \frac{3Fl}{2wh^2} \tag{1}$$

The corresponding flexural strain ε_{fl} for the measured stress is calculated from midspan deflection D according to:

$$\varepsilon_{fl} = 6D\frac{h}{l^2} \tag{2}$$

where F is the force measured by the DMA, l is the load span of the setup (fixed at 50 mm), w is the width and h is the thickness of the specimen. All strain values given in this manuscript are given in percent.

The flexural strength $f_{ct,fl}$ is derived from the highest force measured during mechanical testing. As the basis for dynamic measurements, the mean value of $f_{ct,fl}$ is calculated from a set of 5 specimens.

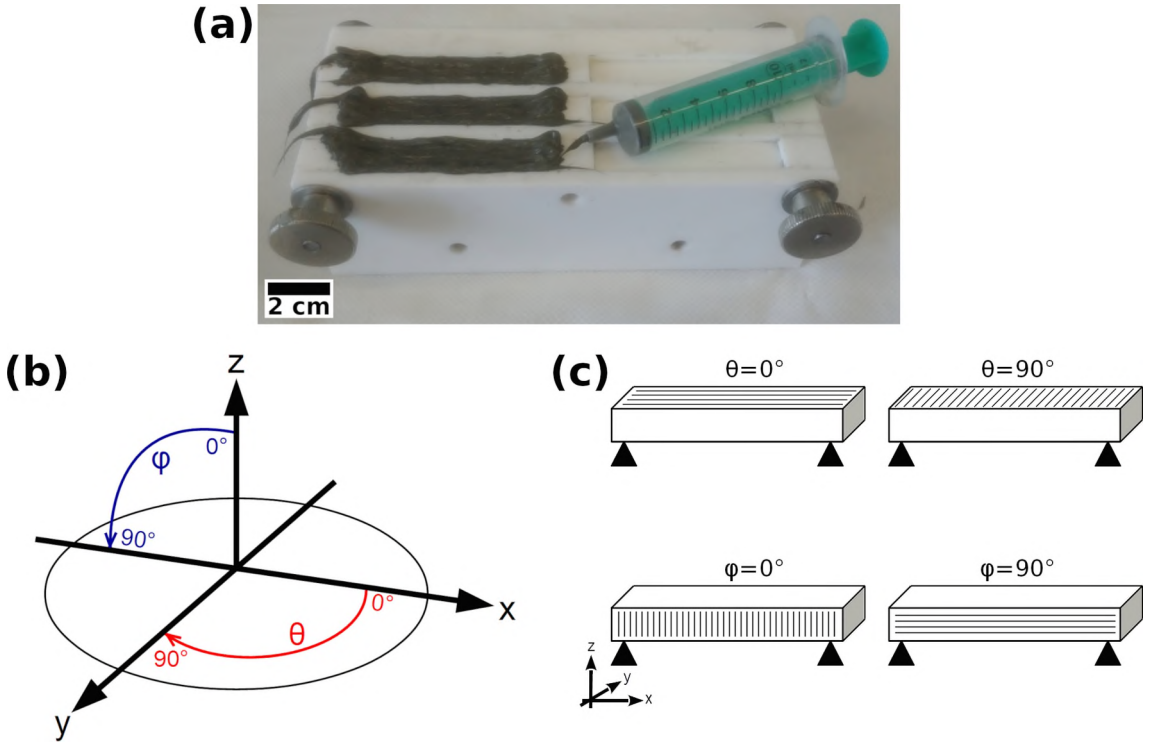

Fig. 2. **(a)** Manual extrusion of the cementitious composite as a means of controlling fiber alignment. **(b)** Three-dimensional coordinate system used to describe fiber alignment in plane (θ-angle) and out of plane (φ-angle). **(c)** Orientation of samples within this coordinate system during flexural testing.

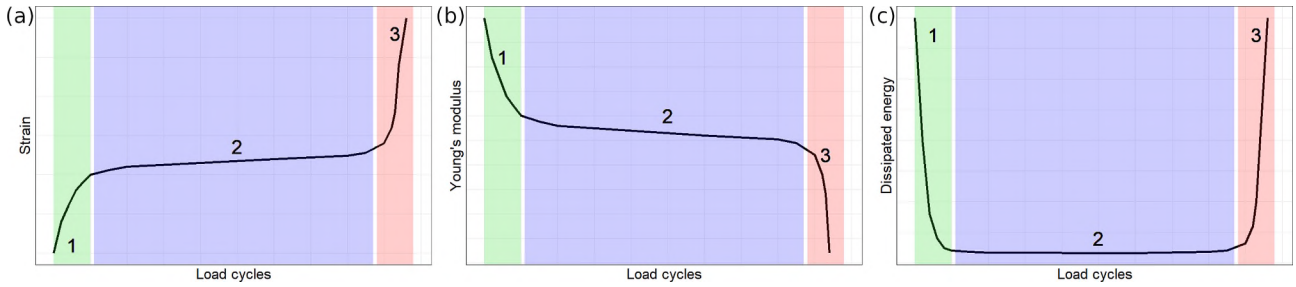

Fig. 3. Idealized development of relevant damage indicators during fatigue testing. **(a)** Development of strain. **(b)** Development of Young's modulus. **(c)** Development of energy dissipation rate. The distinct phases of fatigue development are highlighted in the diagrams. Phase 1 is shaded green, phase 2 is shaded blue and phase 3 is shaded red. (For interpretation of the references to colour in this figure legend, the reader is referred to the web version of this article.)

Table 1
Mixture design used for the preparation of reinforced and unreinforced specimens.

	Dose by weight [wt.-%]	Density [g/cm^3]	Dose by volume [vol.-%]	Mixture design [kg/m^3]
CEM I 52.5 R	58.2	3.10	41.2	1276.4
Silica fume ‚EFACO'	20.0	2.25	19.5	438.6
Barium sulfate	4.6	4.50	2.2	100.9
Deionized water	14.3	1.00	31.4	313.6
MasterGlenium ACE 430	2.9	1.11	5.7	63.6
Addition of carbon fibers for a volume content of 1%:				
Tenax-J HT C261	0.803	1.76	1.0	17.6

Fig. 4. 3-point-bending setup installed in the DMA Q800 with a miniature prism. A 2 Euro coin is shown for scale (diameter: 26 mm).

2.4. Dynamic fatigue measurements

Fatigue tests were performed at 10 Hz using DMA's 'Multi-Frequency-Stress' mode. The different loading regimens derived from the ultimate flexural strength (as described in Section 2.3) can be seen in Table 2. For the lowest stress limits (NR-40 and CF-40), a force of 0.1 N was always maintained to ensure that the specimen did not move during testing.

In addition to more common methods of damage description, such as the development of strain during the fatigue test, a DMA also offers the possibility to assess the elastic and inelastic properties of a material by way of determining the time lag between the applied stress and resulting strain. When applying a cyclical load on a sample, the lag between the applied stress and resulting strain is characteristic of its elasticity and quantified by the phase angle δ. A purely elastic material will show oscillation of stress and strain fully in phase (characterized by $\delta = 0°$, all energy is directly and reversibly transferred into the displacement), a purely viscous material will exhibit oscillation out of phase corresponding to $\delta = 90°$ with all energy put into the material being irreversibly dissipated. Real materials often show behavior between these two extremes and are thus referred to as viscoelastic [34,35]. A diagram of this behavior is shown in Fig. 5.

Once the phase angle δ is known, the material's complex modulus E^* can be calculated. E^* takes the form of a complex number, which can be separated into its real part E' (or storage modulus) and its imaginary part E'' (or loss modulus). E' is a reflection of how elastic a material behaves, while E'' reflects the amount of viscous ('inelastic') behavior within the material. E^*, E' and E'' can be derived when considering different descriptions of oscillating strain ε and oscillating stress σ. Equations (3) to (13) show the relevant calculations based on the values highlighted in Fig. 5 [35].

The time-dependent value of an oscillating strain ε with the (angular) frequency ω can be described as a cosine-function of its strain amplitude ε_0:

$$\varepsilon = \varepsilon_0 \cos\omega t \tag{3}$$

The corresponding oscillating stress σ can be expressed in the same fashion as a combination of the material's Storage Modulus E' and its

Table 2
Upper and lower load levels used for the fatigue tests. Limits are given as absolute values ('absolute stress level') as well as in relation to the material's flexural strength ('relative stress level'). Samples named 'NR' represent specimens without fiber reinforcement, and samples named 'CF' represent specimens reinforced with 1 vol-% carbon fibers.

	Lower load limit		Upper load limit	
	Relative stress level [%]	Absolute stress level [MPa]	Relative stress level [%]	Absolute stress level [MPa]
NR-40	0	0.0	40	6.4
NR-60	20	3.2	60	9.4
NR-80	40	6.4	80	12.5
CF-40	0	0.0	40	25.6
CF-60	20	12.8	60	38.4
CF-80	40	25.6	80	51.2

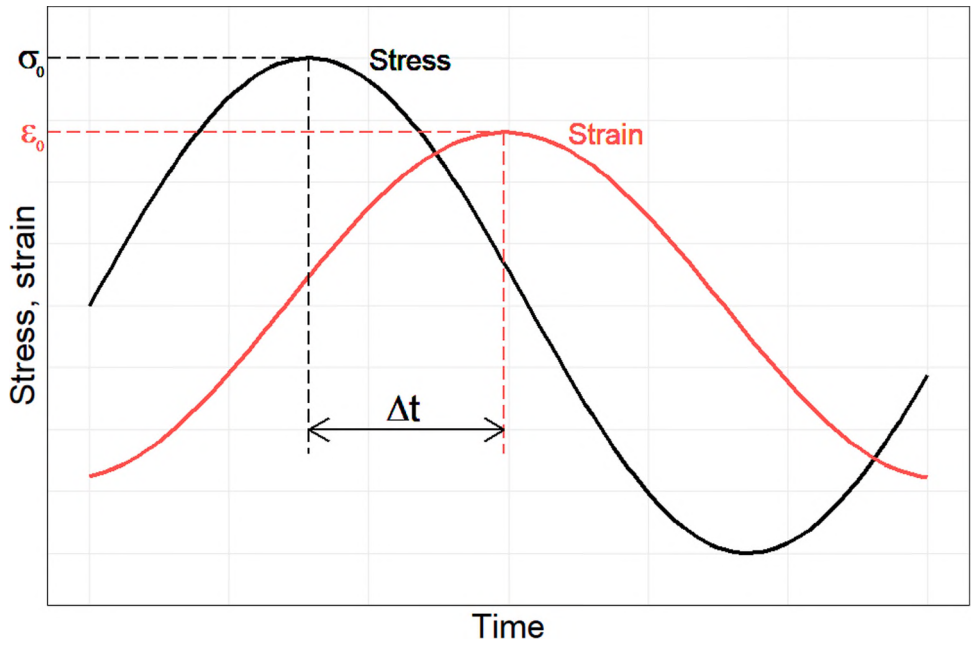

Fig. 5. Model diagram of stress (black) and strain (red) in a viscoelastic material during a measurement with oscillating load. Measuring the time lag between the two signals allows for calculation of the viscoelastic material properties. (For interpretation of the references to colour in this figure legend, the reader is referred to the web version of this article.)

Loss Modulus E'':

$$\sigma = \varepsilon_0(E' \sin(\omega t) + E'' \cos(\omega t)) \tag{4}$$

A very similar description of the oscillating stress can be formulated from its stress amplitude σ_0. As there is a lag between stress and strain in viscoelastic materials, the phase shift δ has to be incorporated into this equation:

$$\sigma = \sigma_0 \sin(\omega t + \delta) = \sigma_0 \cos(\delta)\sin(\omega t) + \sigma_0 \sin(\delta)\cos(\omega t) \tag{5}$$

δ can be obtained from the time lag Δt between stress and strain and the (ordinary) frequency ϑ the cyclical loading experiment is running at:

$$\delta = 2\pi\vartheta\Delta t \tag{6}$$

When equating both descriptions of the oscillating stress, one can see that:

$$E' = \left(\frac{\sigma_0}{\varepsilon_0}\right)\cos\delta \tag{7}$$

$$E'' = \left(\frac{\sigma_0}{\varepsilon_0}\right)\sin\delta \tag{8}$$

$$\frac{E''}{E'} = \tan\delta \tag{9}$$

Using complex notation these descriptions can also be made using complex strain ε^* and complex stress σ^*:

$$\varepsilon^* = \varepsilon_0 \exp i\omega t \tag{10}$$

$$\sigma^* = \sigma_0 \exp i(\omega t + \delta) \tag{11}$$

The complex modulus E^* is given as the relation between complex stress and complex strain. This results in a complex number where the real part defines the Storage Modulus E' and the imaginary part describes the Loss Modulus E'':

$$E^* = \frac{\sigma^*}{\varepsilon^*} = E' + iE'' \tag{12}$$

E' and E'' therefore form a vector in the complex plane describing the magnitude of E^*, which also corresponds to the relation between stress amplitude σ_0 and strain amplitude ε_0:

$$|E^*| = \sqrt{E'^2 + E''^2} = \frac{\sigma_0}{\varepsilon_0} \tag{13}$$

Most commonly, this approach is used to determine the temperature-dependent behavior of thermoplastic materials, especially as a measurement of glass transition points in polymers. However, the method can also be used under isothermal conditions, where a time-resolved evaluation of E' and E'' allows for the identification of processes where elastic or inelastic behavior is especially pronounced. In particular, the noticeable increase and peak of E'' point to occurrences of nonreversible inelastic events such as cracking. The information obtained from this is closely related to the well-established methods of observing Young's modulus (concerning the elastic properties contained within the storage modulus) [27,36] and to the analysis of energy dissipation as calculated by the area of the hysteresis loops (concerning the inelastic properties contained within the loss modulus) [26,37].

2.5. Analysis of fiber alignment and crack growth using X-ray CT

2.5.1. Image acquisition and volume reconstruction

X-ray CT was employed to track microscopic in-volume parameters such as fiber alignment and microcrack development at various stages of cyclic loading experiments without the need for destructive preparation of thin sections. The tomographic measurements were carried out using a Phoenix Nanotom M nano-CT system (GE Inspection Technologies LP, Lewistown, PA, USA). Scans were taken using a beam current of 100 μA and an acceleration voltage of 100 kV. One scan was composed of 2000 single images using an exposure time of 2000 ms. As multiple cracking leads to a large fracture process zone, the miniature prism was scanned 4 times at overlapping positions along its length. The voxel size for every scan was 1 μm. After image acquisition, the raw data were reconstructed using the software 'Phoenix datos|x'. Image geometry was calibrated using the program's 'agc' ('automatic geometry calibration') function. During reconstruction, a ring-artifact reducing filter and a Gaussian filter were applied. The reconstructed scan was saved into raw format and imported into the metrology software ORS Dragonfly Pro 2020.1 (Object Research Systems (ORS) Inc., Montreal, Canada). The voxel size of the scan was scaled down during import by a factor of 2 to lower

computational demand. Within ORS Dragonfly, the overlapping regions were combined using the program's image stitching function to produce a single image, capturing a length of approximately 10 mm around the miniature prism center point where the flexural load was introduced.

2.5.2. *Segmentation procedure*

Carbon fibers are notoriously difficult to segment from a cementitious matrix in a tomographic scan. Due to their small diameter and similar grayscale value, the use of synchrotron CT is often seen as necessary to achieve satisfactory imaging results [38]. Other works focus on leveraging digital image processing techniques to improve contrast and refine segmentations based on fiber geometry [39,40]. The results presented in this publication are segmented using similar principles. The main challenge in segmenting carbon fibers from a cementitious matrix lies in the fact that their respective grayscale values will overlap. As a consequence, the fibers will not be represented by a separated peak in the grayscale value histogram, making segmentation purely based on thresholding infeasible. Instead, the material is passed through a 'local histogram equalization' (LHE) filter. The LHE filter will emphasize local deviations in grayscale value, leaving fibers or cracks as nearly monochromatic black objects within a brighter matrix. This filtering operation allows for threshold-based segmentation with reasonable accuracy. While a significant number of artifacts will still be picked up, they will be mostly isolated from the fibers to be segmented and only composed of a few voxels. Removal of these artifacts is possible by performing a connectivity analysis of the segmented voxels. By combining connected voxels into discrete objects, the accuracy of the segmentation can be improved by excluding objects deviating from the known fiber geometry. Specifically, spherical objects with an aspect ratio approaching 1 and objects with extremely low volume were removed from the segmentation.

3. Results

3.1. *Fiber alignment*

As the alignment of the reinforcing fibers and the mechanical performance of the composite are intrinsically linked [12], further interpretation of mechanical properties has to be coupled with a quantification of fibers aligned in accordance with the acting tensile forces during testing. Fig. 6**a** shows the respective distributions of in-plane alignment angles (θ-angles), and Fig. 6**b** shows the out-of-plane alignment angles (φ-angles) based on data acquired using X-ray CT. The shaded area around the mode value indicates a single-sigma

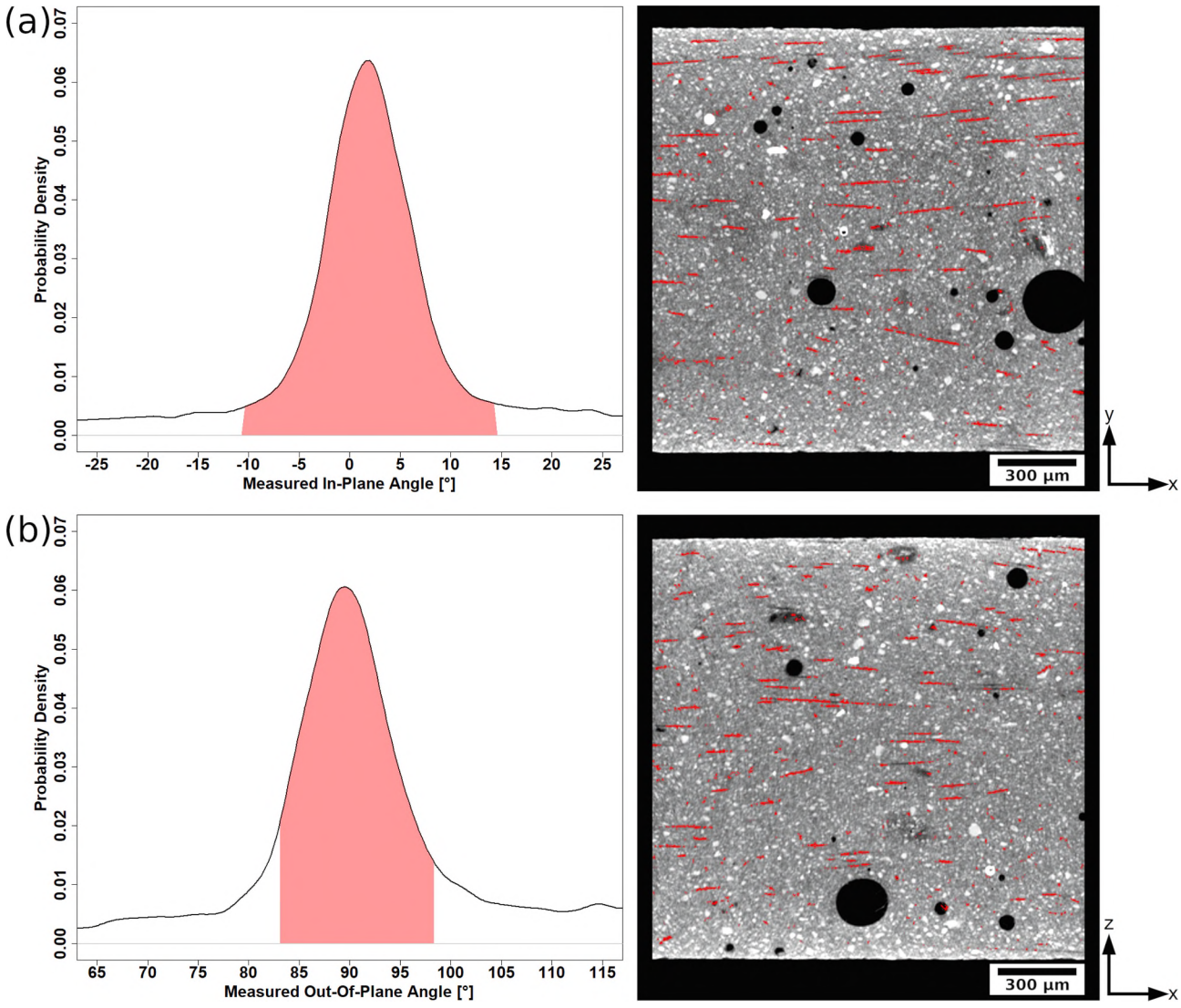

Fig. 6. (a) Distribution of measured in-plane (θ) angles of the segmented fibers (left). Excerpt from the tomographic scan visualizing the fibers and their in-plane alignment (right). **(b)** Distribution of measured out-of-plane (φ) angles of the segmented fibers (left). Excerpt from the tomographic scan visualizing the fibers and their out-of-plane alignment (right).

standard deviation (representing approximately 68% of values present in the dataset) and encompasses the most well-aligned fibers in the respective measurement. Fibers are considered ideally aligned for flexural load when their in-plane alignment is 0° and their out-of-plane alignment is 90°.

As Fig. 6 shows, the extrusion technique is effective in forcing the fibers to align within a narrow preferential angle. Both in-plane and out-of-plane alignment show a mode value of their alignment angle around the desired values of 0° or 90°, respectively. Out-of-plane alignment appears to scatter only slightly, with the standard deviation in Fig. 6**b** encompassing approximately ± 7°, while a slightly higher deviation can be seen in the in-plane angle at approximately ± 12°. Both of these values fall well in line with other publications on this material [11,12].

3.2. Mechanical testing

3.2.1. Determination of static flexural strength

A set of 5 specimens with 1 vol-% fibers as well as without fiber reinforcement was tested to determine their respective flexural strength. The mean of the results acts as the basis for determining the load limits in the dynamic measurements. The results of the static measurements can be seen in Fig. 7.

The effects of the aligned fiber reinforcement are immediately visible in the mechanical response of the material. Unreinforced specimens show a mean flexural strength of 15.7 (±3.3) MPa. The deformation behavior is purely linear elastic until final failure at a deformation between 0.04% and 0.06% flexural strain. Specimens reinforced with 1 vol-% carbon fibers show a greatly improved flexural strength of 64.0 (±8.5) MPa. The specimens are capable of bearing further load even after their linear elastic limits have been reached, as cracks in the cementitious matrix no longer lead to immediate failure. Rather, they are bridged by the fibers, which propagate the load further along the length of the specimen. This process leads to the formation of a multitude of microcracks and is also responsible for the increase in capacity for flexural strain to values of up to 1%. More extensive research on the material's behavior under static loading can be found in Ref. [11,12].

3.2.2. Fatigue life and strain development

The most basic analysis of a material's performance under cyclic loading is assessing the number of load cycles the material can withstand at a given level of stress. Plotting these two parameters results in what is known as a Woehler diagram or stress-life (S-N) diagram. Fig. 8 shows the contrast in lifetime between specimens with 1 vol-% carbon fibers and specimens without reinforcement. For reasons of comparability, the stress level in the diagram is normalized to each material's flexural strength (see also Table 2). The curves in Fig. 8 represent a linear regression through the individual fatigue experiments (represented by the dots). The grey ribbon around the regression line indicates the 95% confidence interval of the regression.

The reinforced specimens show a vastly improved lifetime under cyclic loading. The unreinforced specimens can withstand between several thousand cycles at an upper stress level of 80% of their flexural strength (12.5 MPa, loading regimen NR-80 in Table 2) and several hundred thousand cycles at an upper stress level of 40% flexural strength (6.4 MPa, loading regimen NR-40 in Table 2). The carbon fiber-reinforced specimens show a lifetime just short of a million load cycles at an upper stress level of 80% flexural strength (51.2 MPa, loading regimen CF-80 in Table 2) and between 5 and 9 million load cycles at 40% flexural strength (25.6 MPa, loading regimen CF-80 in Table 2).

This vast increase in service life is especially remarkable, when considering that the reinforced specimens actually carry a significantly higher load. As the load S-N curve is normalized, the absolute load on the reinforced specimens is approximately 4 times higher than on the unreinforced specimens. It is also notable that for the case of the fiber-reinforced specimens, all loading scenarios have their upper load level in the strain-hardening region of the stress–strain diagram (cf. Fig. 7), meaning that this level of performance is achieved with microcracks present from the beginning of the test.

While the accuracy of the S-N curves needs some more refinement when looking at possible applications of the material for engineering purposes, the vast difference in service life between reinforced and unreinforced specimens allows for a number of conclusions: As the two

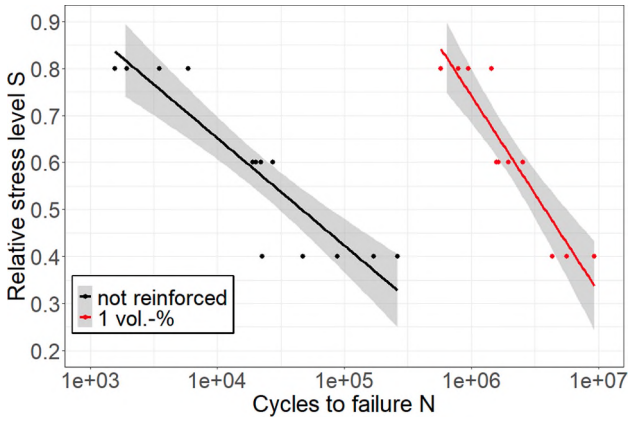

Fig. 8. S-N diagrams showing fatigue behavior for unreinforced specimens (black) and specimens reinforced with 1 vol-% carbon fibers (red). The gray area around the regression lines indicates a confidence interval of 95%. (For interpretation of the references to colour in this figure legend, the reader is referred to the web version of this article.)

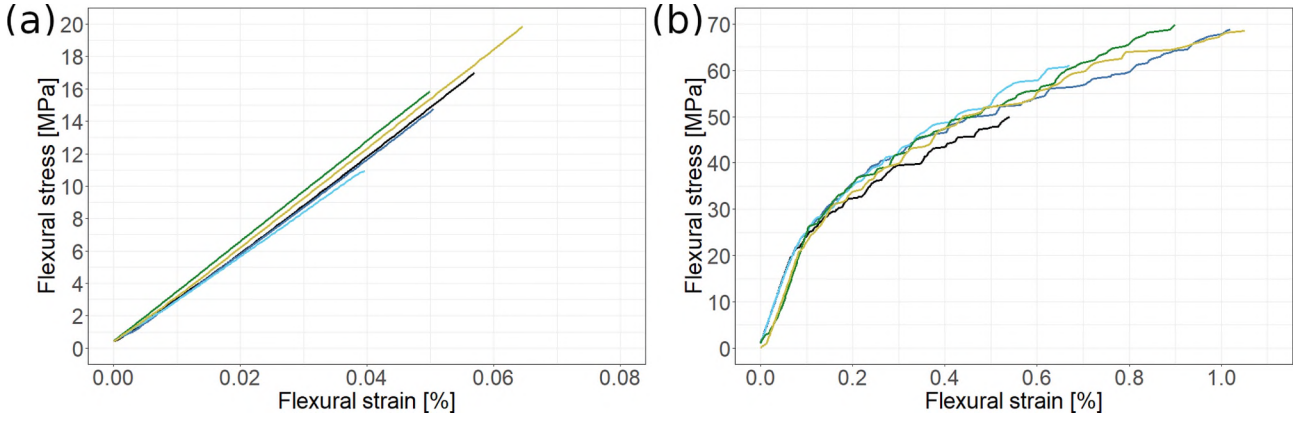

Fig. 7. Stress–strain diagrams of the static mechanical test to determine the flexural strength of the miniature prisms. **(a)** Unreinforced specimens. **(b)** Specimens reinforced with 1 vol-% carbon fibers.

regression lines follow vastly different paths, it is highly probable that the introduction and development of fatigue damage is mechanistically different between unreinforced and reinforced specimens. This is confirmed when comparing the development of strain (measured at the respective upper stress limit) for reinforced and unreinforced specimens during a fatigue test. Fig. 9 shows the contrast between the deformation behavior of two respective miniature prisms at a maximum relative stress level of 60% (see load regimens NR-60 and CF-60 in Table 2). As the absolute numbers for both strain and cycles until failure are vastly different for both specimens, strain has been normalized to the strain-at-break and the cycle number to cycles until failure for the sake of comparability. The resulting graph shows how much of the material capacity for deformation has been used up at each stage of fatigue.

Fig. 9 confirms that the reinforced prism shows a rapid increase in early deformation, reaching approximately 65% of its strain capacity after 20% of its lifetime, after which the strain development starts leveling off slowly. After the reinforced specimen reaches just above 90% strain capacity, the specimen starts failing rapidly within a few cycles. Unreinforced specimens show considerably less early deformation (approximately 20% of strain capacity at 20% of its lifetime), with a steadier strain increase in phase 2 of the fatigue process. Ultimate failure occurs quickly and suddenly for both the reinforced and unreinforced specimens.

It is likely that this is driven by the different mechanisms of fracture governing the failure of the reinforced and unreinforced specimens. While the unreinforced miniature prisms fail due to brittle fracture once a single critical crack has been introduced, the reinforced prisms can accumulate several stable microcracks before failing. Hence, the low deformation of the unreinforced prisms in phase 1 can be read as a single crack being introduced that is steadily growing (phase 2, starting at a cycle ratio of approximately 0.15) until the crack reaches a critical length that leads to instant failure (phase 3). In contrast, the reinforced specimens will saturate themselves with multiple microcracks early, leading to prolonged phase 1 with massive deformation. Once a cycle ratio of approximately 0.25 is reached, crack growth is likely hindered by fiber bridging, leading to a very stable and uneventful phase 2 until fatigue damage progresses to the point where one of the cracks grows above the critical length and the specimen fails (phase 3).

3.2.3. *Viscoelastic parameters as damage indicators*

As the fiber-reinforced specimens show unusual behavior under cyclical loading, we aim to extract additional information from their viscoelastic behavior to better understand the mechanisms governing their specific failure modes. To this end, the storage and loss moduli were measured during cyclical loading, and their development can be seen in Fig. 10.

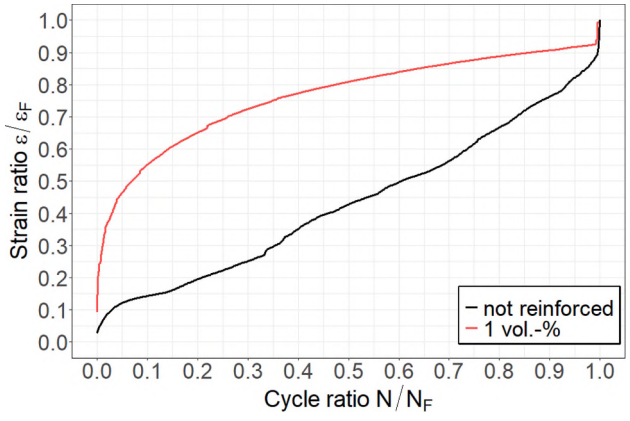

Fig. 9. Strain ratio (strain ε normalized to strain-at-break ε_F) and cycle ratio (load cycle N normalized to cycles until failure N_F) for unreinforced specimens (black) and specimens with 1 vol-% carbon fibers (red) loaded according to regimens NR-60 and CF-60 (see Table 2). Strain was measured at the upper stress limit of the respective loading regimen CF-60 or NR-60. (For interpretation of the references to colour in this figure legend, the reader is referred to the web version of this article.)

Looking purely at the elastic properties represented by the storage modulus, the 3-phase structure of the fatigue process is hard to predict. This is due to similar reasons as discussed in the strain development seen in Fig. 9. While the storage modulus generally follows the expected S-curve and the transition from phase 1 to phase 2 can be discerned well, the transition from phase 2 to phase 3 occurs in a seemingly very short timeframe, with failure occurring just after a few load cycles.

However, an analysis of the loss modulus allows for a significantly greater predictability of the progressing damage within the material. Phase 1 is visible as a steep decline in the loss modulus that slowly levels out, as large amounts of energy are dissipated in the beginning when the first cracks are formed. Phase 2 manifests itself as the loss modulus remaining at an approximately constant level. In phase 3, the loss modulus will start rising again. In addition, discontinuous spiking of the loss modulus can often be observed, which is especially visible in Fig. 10**a** and Fig. 10**b**. Looking at both the storage modulus and loss modulus, phase 3 is marked by a decline in the storage modulus, while the loss modulus starts increasing.

While the final rise in the loss modulus before ultimate failure falls within a shorter window, with a higher load level, even at a stress level of 80%, the first indications of entering phase 3 can be seen approximately 200,000 cycles before failure. In the case of a 40% stress level, phase 3 can be seen starting 1.5 million load cycles before final failure. Both cases leave potentially enough time for preemptive measures, as failure can be predicted early.

3.3. *Observation of crack growth during fatigue testing*

In addition to the continuous loading performed in the experiments in Section 3.2, a fiber-reinforced specimen was loaded discontinuously (according to loading regimen CF-60, see Table 2) for a set number of cycles, removed from the DMA. The midpoint of the specimen was then scanned for structural damage using X-ray CT and reinserted into the flexural setup. This process was repeated until the specimen failed, after which it was scanned once more to assess the postfailure damage. Microcracks segmented from the CT data after each respective step are shown in Fig. 11.

Visible fatigue damage mostly manifests itself by an increasing number of cracks, most of which appear early during the specimen's lifetime. The cracking patterns visible in Fig. 11 suggest that once a microcrack has developed in the material, the crack length and width remain relatively constant; further load cycles lead to the formation of more microcracks instead. This is in accordance with the models proposed for the mechanical behavior of SHCCs, where such behavior has often times been seen for static loads [2,41–43]. After approximately 100,000 load cycles (24% of the specimen's fatigue life), crack formation appears to be mostly complete (see the difference between Fig. 11**c** and Fig. 11**d**). Interestingly, this marks a similar value to the point at which strain development in Fig. 9 starts leveling off, suggesting that the macroscopic deformation is caused by microcracking, as discussed in Section 3.2.2. Once the specimen is saturated with microcracks, the deformation of the specimen will slow considerably.

All microcracks visible in Fig. 11 pass straight through the miniature beam and appear to be isolated from each other. Damage mechanisms such as crack deflection (inclined or kinked crack growth due to debonding at the fiber–matrix interface) or formation of a crack network could not be observed, as they either play no role in early fatigue or are below the resolution of the tomograph. Table 3 shows the crack distance as well as the number of cracks for each scan taken. The crack distance is calculated from the point-to-point distance of each crack's center of mass.

In contrast to the cracks being mostly isolated during testing, the

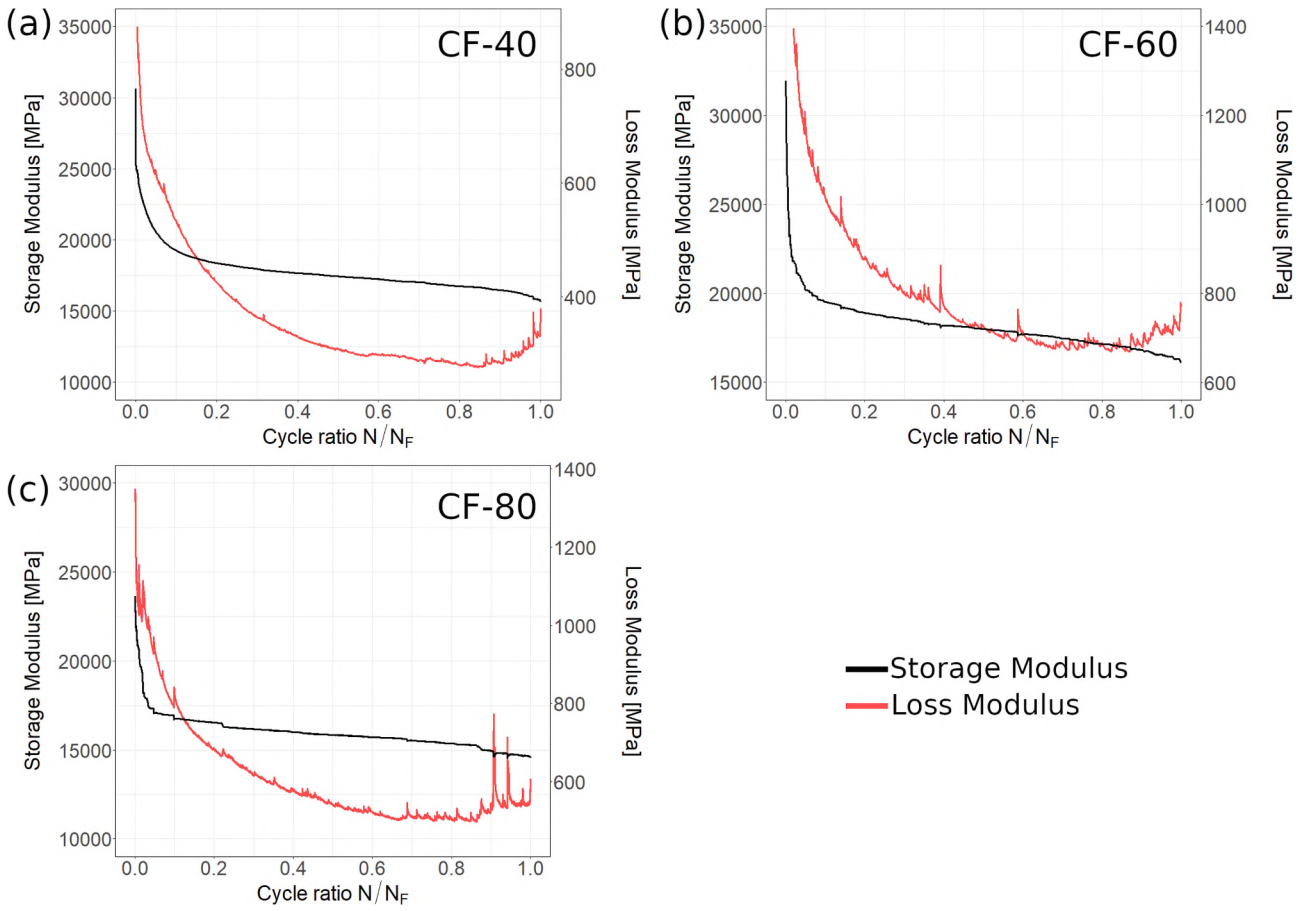

Fig. 10. Typical development of storage modulus (black) and loss modulus (red) when testing samples with the parameters **(a)** CF-40 (failure after 5,640,169 cycles), **(b)** CF-60 (failure after 1,966,480 cycles) and **(c)** CF-80 (failure after 945,444 cycles), as described in Table 2. (For interpretation of the references to colour in this figure legend, the reader is referred to the web version of this article.)

macrocrack that leads to ultimate failure shows obvious signs of crack deflection (Fig. 11**d**). Its path meanders through the specimen, and it appears to have formed from at least two neighboring cracks growing into each other. Cross-referencing these findings with the development of the loss modulus seen in Fig. 10 allows the conclusion that early dissipation of energy during testing is correlated to the formation of an increasing number of microcracks. As the specimen is saturated with stable microcracks, less energy is dissipated, and fatigue enters the steady state of phase 2. Toward the end of the specimen's lifetime, an increase in energy dissipation can be observed. Cross-referencing this with the crack development seen in Fig. 11 suggests a correlation of this energy dissipation with the unification of multiple small cracks into one fatal crack. Other irreversible events that are below the resolution limit of the X-ray CT, such as fiber slippage or failure at the interface, should also be considered as possible contributions to the dissipated energy visible once the specimen enters phase 3 of fatigue. Effects on this level have recently been observed by Ranjbarian and Mechtcherine, who found permanent damage of the fibers (especially effects such as abrasion and defibrillation) when testing for the bridging behavior of polymeric single fibers under cyclical alternating tensile-compressive load as fibers in the crack would start buckling [44–46]. Irreversible damage, as observed in these studies, would also be expected to appear as energy dissipation and thus be correlated to an increasing loss modulus, as seen in late-stage fatigue. The fact that the final failure occurred at a crack that developed relatively late into testing is also remarkable. Such effects have often been observed and discussed in static loading of SHCC specimens and seem to carry over into the field of cyclic loading as well [47]. The inclined path of the final crack also suggests that it is possibly a result of mixed-mode or shear load occurring towards the very end of the fatigue experiments. As the fiber reinforcement is tailored towards resisting tensile loads, these loading types are likely to lead to sudden critical crack growth and failure of the specimen.

4. Conclusion

By using an extrusion-based process, additive manufacturing of cementitious composites with aligned carbon fibers is possible. In addition to a vastly improved static flexural strength and strain hardening-induced toughness, composites with aligned carbon fibers show a significantly longer service life under cyclic loading than specimens made from unreinforced matrix materials, as the number of cycles to failure increases from tens of thousands to several million at the same relative stress level. In contrast to regular cementitious materials, which show instant brittle failure, the composites are characterized by the formation of multiple stable microcracks before final failure. When testing above the composites beyond their linear-elastic capabilities, phase 1 fatigue is prolonged when compared to unreinforced specimens. The development of damage during phase 1 is characterized by early saturation with microcracks that go hand in hand with massive deformation of the specimen. Once this early damage has been introduced, strain development in phase 2 appears stable and uneventful until phase 3 sets suddenly, causing ultimate failure of the specimen with little prior warning. Looking at multiple indicators allows for more predictability when interpreting fatigue behavior. In particular, analysis of the viscoelastic behavior of the material allows for early recognition of phase 3, as the material will show a steady increase in loss modulus (and thus dissipation of energy) starting some hundred thousand cycles before failure. This behavior is confirmed by X-ray CT scans, showing early

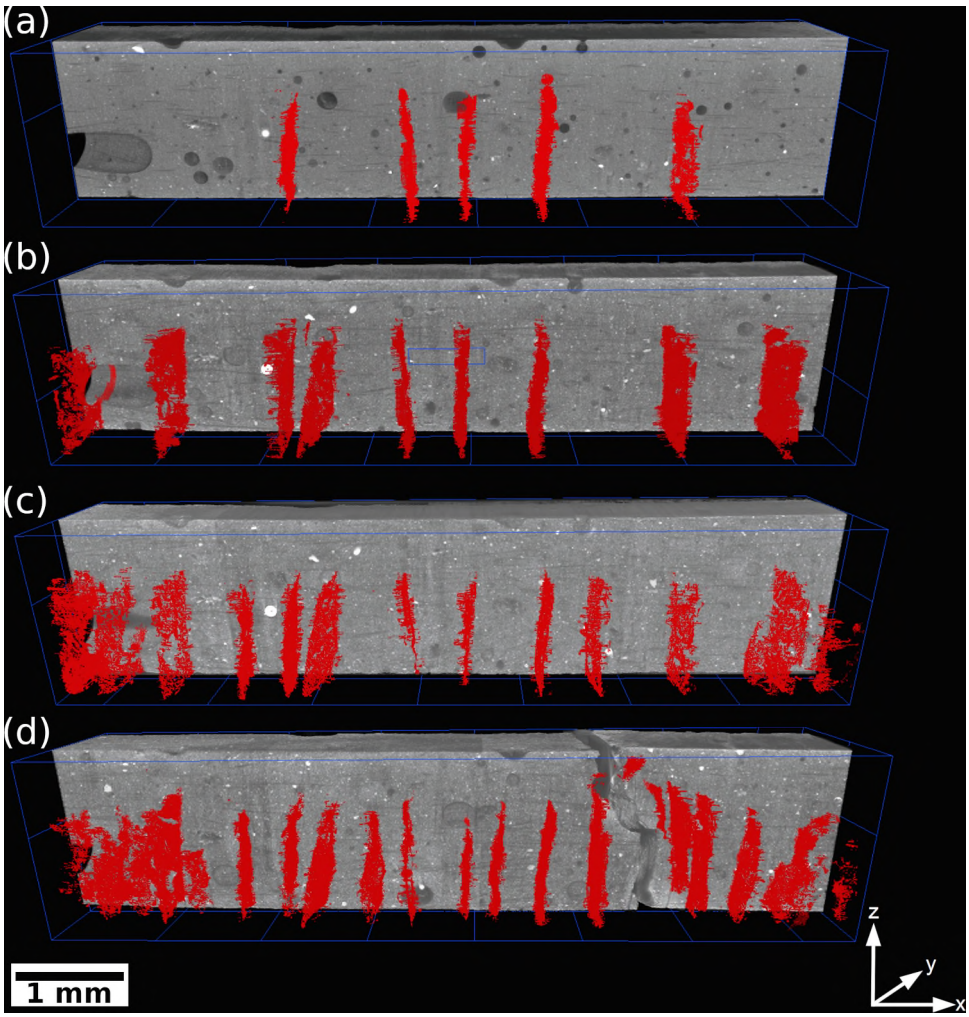

Fig. 11. Development of cracks in a specimen loaded according to regimen CF-60 (see Table 2) after **(a)** 773 load cycles (0.2% of the sample's lifetime), **(b)** 9,535 load cycles (2.3% of the sample's lifetime), **(c)** 99,289 load cycles (24.4% of the sample's lifetime) and **(d)** complete failure (406,710 load cycles). The figure shows the crack development within the are directly located under the loading pin and thus the immediate fracture process zone.

Table 3
Number of cracks and cracked distance (crack distance resolved with an accuracy of 10 μm) measured in the segmentation of the miniature prism visible in Fig. 11.

Load cycles	Mean crack distance [μm]	Number of segmented cracks
773	930 (±360)	5
9,535	840 (±290)	9
99,289	550 (±190)	15
406,710	400 (±160)	23

introduction of numerous separated microcracks, which appear to unify into a macrocrack before ultimate failure.

As the material shows promising levels of performance under monotonic cyclic loading, further investigations into fatigue under changing stress levels and amplitudes seem prudent given that the starting conditions of a fatigue experiment will play an important role in how many microcracks are introduced into the specimen and how damage will accumulate on them during its service life. Determination of fatigue behavior under different types of loads, especially testing the behavior under pure centric tensile loading and alternating tensile and compressive loading, promises interesting results. Furthermore, more research on the impact of damage occurring on the single-fiber scale (pull-out, fiber breakage, etc.) would lead to a better understanding of the behavior shown in phase 3 of fatigue.

Funding

This research was funded by the German Research Foundation DFG as part of the 'Priority Programme SPP 2020: Cyclic deterioration of High-Performance Concrete in an experimental-virtual lab' (grant number VO 829/13–1).

Availability of data and material

Raw data are available from the authors upon request.

Code availability

Not applicable.

Author contributions

All research presented in this study was performed by the Chair of Solid State and Materials Chemistry.

Declaration of Competing Interest

The authors declare that they have no known competing financial interests or personal relationships that could have appeared to influence the work reported in this paper.

Acknowledgements

The researchers would like to express their heartfelt thanks to everyone participating in the Priority Programme 'SPP 2020: Cyclic deterioration of High-Performance Concrete in an experimental-virtual lab' for all the invaluable discussion and scientific input received during the project runtime.

Furthermore, we would like to thank Schwenk Zement KG, Mr. Thomas Neumann and Dr. Hendrik Möller in particular for kindly supplying the cement used in this research.

References

[1] Zollo RF. Fiber-reinforced concrete: an overview after 30 years of development. Cem Concr Comp 1997;19(2):107–22. https://doi.org/10.1016/S0958-9465(96)00046-7.
[2] Li VC. On Engineered Cementitious Composites (ECC). J Adv Concr Technol 2003;1(3):215–30. https://doi.org/10.3151/jact.1.215.
[3] Li VC, Wu C, Wang S, Ogawa A, Saito T. Interface tailoring for strain-hardening polyvinyl alcohol-engineered cementitious composite (PVA-ECC). ACI Mater J 2002;99(5):463–72.
[4] Li VC, Leung CKY. Steady-State and Multiple Cracking of Short Random Fiber Composites. J Eng Mech 1992;118(11):2246–64. https://doi.org/10.1061/(ASCE)0733-9399(1992)118:11(2246).
[5] Li VC, Wang S, Wu C. Tensile strain-hardening behavior of polyvinyl alcohol engineered cementitious composite (PVA-ECC). ACI Mater J 2001;98(6):483–92.
[6] Jun P, Mechtcherine V. Behaviour of Strain-hardening Cement-based Composites (SHCC) under monotonic and cyclic tensile loading. Cem Concr Comp 2010;32(10):801–9. https://doi.org/10.1016/j.cemconcomp.2010.07.019.
[7] Li VC, Herbert E. Robust Self-Healing Concrete for Sustainable Infrastructure. J Adv Concr Technol 2012;10(6):207–18. https://doi.org/10.3151/jact.10.207.
[8] Sherir MA, Hossain KM, Lachemi M. Self-healing and expansion characteristics of cementitious composites with high volume fly ash and MgO-type expansive agent. Constr Build Mater 2016;127:80–92. https://doi.org/10.1016/j.conbuildmat.2016.09.125.
[9] Zhang P, Dai Y, Ding X, Zhou C, Xue X, Zhao T. Self-healing behaviour of multiple microcracks of strain hardening cementitious composites (SHCC). Constr Build Mater 2018;169:705–15. https://doi.org/10.1016/j.conbuildmat.2018.03.032.
[10] van Zijl GPAG, Wittmann FH, Oh BH, Kabele P, Toledo Filho RD, Fairbairn EMR, et al. Durability of strain-hardening cement-based composites (SHCC). Mater Struct 2012;45(10):1447–63. https://doi.org/10.1617/s11527-012-9845-y.
[11] Hambach M, Möller H, Neumann T, Volkmer D. Portland cement paste with aligned carbon fibers exhibiting exceptionally high flexural strength (> 100 MPa). Cem Concr Res 2016;89:80–6. https://doi.org/10.1016/j.cemconres.2016.08.011.
[12] Rutzen M, Lauff P, Niedermeier R, Fischer O, Raith M, Grosse CU, et al. Influence of fiber alignment on pseudoductility and microcracking in a cementitious carbon fiber composite material. Mater Struct 2021;54(2). https://doi.org/10.1617/s11527-021-01649-2.
[13] Kanarska Y, Duoss EB, Lewicki JP, Rodriguez JN, Wu A. Fiber motion in highly confined flows of carbon fiber and non-Newtonian polymer. J Non-Newton Fluid 2019;265:41–52. https://doi.org/10.1016/j.jnnfm.2019.01.003.
[14] Hambach M, Volkmer D. Properties of 3D-printed fiber-reinforced Portland cement paste. Cem Concr Comp 2017;79:62–70. https://doi.org/10.1016/j.cemconcomp.2017.02.001.
[15] Lewicki JP, Rodriguez JN, Zhu C, Worsley MA, Wu AS, Kanarska Y, et al. 3D-Printing of Meso-structurally Ordered Carbon Fiber/Polymer Composites with Unprecedented Orthotropic Physical Properties. Sci Rep 2017;7(1). https://doi.org/10.1038/srep43401.
[16] Soltan DG, Li VC. A self-reinforced cementitious composite for building-scale 3D printing. Cem Concr Comp 2018;90:1–13. https://doi.org/10.1016/j.cemconcomp.2018.03.017.
[17] Lauff P, Fischer O. Effizienter Ultrahochleistungsbeton mit innovativer trajektorienorientierter „Bewehrung". ce/papers 2019;3(2):82–8. https://doi.org/10.1002/cepa.976.
[18] Chung D. Cement reinforced with short carbon fibers: a multifunctional material. Compos Part B - Eng 2000;31(6–7):511–26. https://doi.org/10.1016/S1359-8368(99)00071-2.
[19] Hambach M, Möller H, Neumann T, Volkmer D. Carbon fibre reinforced cement-based composites as smart floor heating materials. Compos Part B - Eng 2016;90:465–70. https://doi.org/10.1016/j.compositesb.2016.01.043.
[20] Müller S, Mechtcherine V. Fatigue behaviour of strain-hardening cement-based composites (SHCC). Cem Concr Res 2017;92:75–83. https://doi.org/10.1016/j.cemconres.2016.11.003.
[21] Mueller S, Ranjbarian M, Mechtcherine V. Fatigue behavior of strain-hardening cement-based composites—From the single fiber level to real-scale application. Struct Concr 2019;20(4):1231–42. https://doi.org/10.1002/suco.201900032.
[22] Scheerer S, Chudoba R, Garibaldi MP, Curbach M. Shells Made of Textile Reinforced Concrete - Applications in Germany. J Int Assoc Shell Spat Struct 2017;58(1):79–93. https://doi.org/10.20898/j.iass.2017.191.846.
[23] Rempel S, Will N, Hegger J, Beul P. Filigrane Bauwerke aus Textilbeton. Beton-Stahlbetonbau 2015;110(S1):83–93. https://doi.org/10.1002/best.201400111.
[24] Oneschkow N. Fatigue behaviour of high-strength concrete with respect to strain and stiffness. Int J Fatigue 2016;87:38–49. https://doi.org/10.1016/j.ijfatigue.2016.01.008.
[25] Hordijk DA, Wolsink GM, DeVries J. Fracture and fatigue behavior of a high strength limestone concrete as compared to gravel concrete. Heron 1995;40(2):125–46.
[26] Ghuzlan KA, Carpenter SH. Energy-Derived, Damage-Based Failure Criterion for Fatigue Testing. Transp Res Record 2000;1723(1):141–9. https://doi.org/10.3141/1723-18.
[27] Kessler-Kramer C. Zugtragverhalten von Beton unter Ermüdungsbeanspruchung [Karlsruhe, Univ., Diss., 2002]. Karlsruhe: KIT-Bibliothek; 2002.
[28] Fitik B. Ermüdungsverhalten von ultrahochfestem Beton (UHPC) bei zyklischen Beanspruchungen im Druck-Zug-Wechselbereich [München, Technische Universität München, Diss., 2012]. München: Universitätsbibliothek der TU München; 2012.
[29] Baktheer A, Chudoba R. Experimental and theoretical evidence for the load sequence effect in the compressive fatigue behavior of concrete. Mater Struct 2021;54(2). https://doi.org/10.1617/s11527-021-01667-0.
[30] Paris P, Erdogan F. A Critical Analysis of Crack Propagation Laws. J Basic Eng 1963;85(4):528–33. https://doi.org/10.1115/1.3656900.
[31] Lee MK, Barr B. An overview of the fatigue behaviour of plain and fibre reinforced concrete. Cem Concr Comp 2004;26(4):299–305. https://doi.org/10.1016/S0958-9465(02)00139-7.
[32] Lohaus L, Anders S. High-cycle Fatigue of "Ultra-High Performance Concrete" and "Grouted Joints" for Offshore Wind Energy Turbines. In: Peinke J, Schaumann P, Barth S, editors. Wind Energy. Springer, Berlin Heidelberg: Berlin, Heidelberg; 2007. p. 309–12.
[33] Carrara P, Kruse R, Bentz DP, Lunardelli M, Leusmann T, Varady PA, et al. Improved mesoscale segmentation of concrete from 3D X-ray images using contrast enhancers. Cem Concr Comp 2018;93:30–42. https://doi.org/10.1016/j.cemconcomp.2018.06.014.
[34] Lakes RS. Viscoelastic materials. New York: Cambridge University Press; 2014.
[35] Ferry JD. Viscoelastic properties of polymers. 3rd ed. New York, Chichester: Wiley; 1980.
[36] Hohberg R. Zum Ermüdungsverhalten von Beton. Technische Universität Berlin 2004.
[37] Shen S, Airey GD, Carpenter SH, Huang H. A Dissipated Energy Approach to Fatigue Evaluation. Road Mater Pavement 2006;7(1):47–69. https://doi.org/10.1080/14680629.2006.9690026.
[38] Sencu RM, Yang Z, Wang YC, Withers PJ, Rau C, Parson A, et al. Generation of micro-scale finite element models from synchrotron X-ray CT images for multidirectional carbon fibre reinforced composites. Compos Part A - Appl S 2016;91:85–95.
[39] Oesch T, Landis E, Kuchma D. A methodology for quantifying the impact of casting procedure on anisotropy in fiber-reinforced concrete using X-ray CT. Mater Struct 2018;51(3). https://doi.org/10.1617/s11527-018-1198-8.
[40] Oesch T, Stelzner L, Weise F. Non-destructive Evaluation of the Contribution of Polymer-Fibre Orientation and Distribution Characteristics to Concrete Performance during Fire. In: Herrmann H, Schnell J, editors. Short Fibre Reinforced Cementitious Composites and Ceramics. Cham: Springer International Publishing; 2019. p. 51–73.
[41] Kanada T, Li VC. Multiple Cracking Sequence and Saturation in Fiber Reinforced Cementitious Composites. Concr Res Technol 1998;9(2):19–33. https://doi.org/10.3151/crt1990.9.2_19.
[42] Kanda T, Li VC. Practical Design Criteria for Saturated Pseudo Strain Hardening Behavior in ECC. J Adv Concr Technol 2006;4(1):59–72. https://doi.org/10.3151/jact.4.59.
[43] Li J, Qiu J, He S, Yang E-H. Micromechanics-Based Design of Strain Hardening Cementitious Composites (SHCC). In: Mechtcherine V, Slowik V, Kabele P, editors. Strain-Hardening Cement-Based Composites. Dordrecht: Springer Netherlands; 2018, p. 12–27.
[44] Ranjbarian M, Mechtcherine V. A novel test setup for the characterization of bridging behaviour of single microfibres embedded in a mineral-based matrix. Cem Concr Comp 2018;92:92–101. https://doi.org/10.1016/j.cemconcomp.2018.05.017.
[45] Ranjbarian M, Mechtcherine V. Influence of loading parameters in cyclic tension-compression regime on crack-bridging behaviour of PVA microfibres embedded in cement-based matrix. Constr Build Mater 2019;228:116760. https://doi.org/10.1016/j.conbuildmat.2019.116760.
[46] Ranjbarian M, Ma X, Mechtcherine V. Influence of Crack Width in Alternating Tension-Compression Regimes on Crack-Bridging Behaviour and Degradation of PVA Microfibres Embedded in Cement-Based Matrix. Materials (Basel) 2020;13(18):4189. https://doi.org/10.3390/ma13184189.
[47] Yu J. Why nominal cracking strength can be lower for later cracks in strain-hardening cementitious composites with multiple cracking? In: Proceedings of the 10th International Conference on Fracture Mechanics of Concrete and Concrete Structures. IA-FraMCoS; 2019.